Wind and Structures, Volume 34, Issue 6, June 2022, pp. 483-497
DOI:10.12989/was.2022.34.6.483

A 3D CFD analysis of flow past a hipped roof with comparison to industrial building standards

Khalid Khalil[a], Huzafa Khan[b], Divyansh Chahar[c], Jamie F. Townsend[*] and Zeeshan A. Rana[d]

Centre for Computational Engineering Sciences, Cranfield University, Cranfield, Bedfordshire, MK43 0AL, United Kingdom

(*Received December 4, 2021, Revised March 30, 2022, Accepted May 15, 2022*)

Abstract. Three-dimensional (3D) computational fluid dynamics (CFD) analysis of flow around a hipped-roof building representative of UK inland conditions are conducted. Unsteady simulations are performed using three variations of the k–ϵ RANS turbulence model namely, the Standard, Realizable, and RNG models, and their predictive capability is measured against current European building standards. External pressure coefficients and wind loading are found through the BS 6399-2:1997 standard (obsolete) and the current European standards (BS EN 1991-1-4:2005 and A1:20101). The current European standard provides a more conservative wind loading estimate compared to its predecessor and the k–ϵ RNG model falls within 15% of the value predicted by the current standard. Surface shear stream-traces and Q-criterion were used to analyze the flow physics for each model. The RNG model predicts immediate flow separation leading to the creation of vortical structures on the hipped-roof along with a larger separation region. It is observed that the Realizable model predicts the side vortex to be a result of both the horseshoe vortex and the flow deflected off it. These model-specific aerodynamic features present the most disparity between building standards at leeward roof locations. Finally, pedestrian comfort and safety criteria are studied where the k–ϵ Standard model predicts the most ideal pedestrian conditions and the Realizable model yields the most conservative levels.

Keywords: CFD (Computational Fluid Dynamics); design codes and standards; pedestrian wind comfort; steady/ unsteady aerodynamic force; turbulence; wind loads

1. Introduction

Understanding the impact of wind on buildings and its pressure-distribution is a vital aspect of modern-day building design. As such, civil engineers have utilized computational fluid dynamics (CFD) to investigate the pressure-distribution and wind loading on various building configurations (Blocken 2014). These studies typically make use of Reynolds-Averaged Navier–Stokes (RANS) turbulence modeling practices which represent the most widely used methodology for insights into turbulent flow. Extensive studies have been performed for external aerodynamics applications concerning low-rise gable roof houses by Montazeri and Blocken (2013), Tominaga *et al*. (2015), Ozmen *et al*. (2016) and internal flow such as building ventilation by Perén *et al*. (2015). Gaining practical insight into the fidelity of CFD data can also improve decision-making in the urban design process regarding pedestrian wind comfort levels (Fernando *et al*. 2020). Other CFD studies of a similar nature consider a Large-Eddy Simulation (LES) strategy and indicate a performance advantage in terms of realizing fluctuating pressures on a building geometry, see Zheng *et al*. (2020) and references therein. This is in part due to the fact that unsteady flow characteristics are present for building geometries such that a steady-state approach can lack important aerodynamic detail (Amini and Memari 2021). CFD can also be leveraged to further understand aerodynamics for larger-scale infrastructure in regions with geographically complicated terrain such as in a mountainous region which is characterized by unsteady aerodynamics (Han *et al*. 2018). Although LES presents certain advantages over RANS, computational cost and a lack of best practice guidelines can hinder successful applications of this technology (Blocken 2018). The numerical investigations are often complemented with experimental data to enhance their validity and provide insight into the behavior of CFD techniques such as the choice of turbulence model. Due to the turbulent behavior of wind flow within urban areas, research has been performed to assess the impact of these micro-climatic conditions on human comfort and safety (Stathopoulos 2006, Xu *et al*. 2017). The Architectural Institute of Japan (AIJ) (Tominaga *et al*. 2008b) composed a set of guidelines based on comparison studies between CFD and wind tunnel data, which included seven separate test cases, representing different urban scenarios. While instantaneous wind speed is a critical parameter to consider in a comfort index (to account for wind gusts), it is argued that mean wind speeds are sufficient for major cities, along with a specified probability of exceedance. RANS modeling is extensively used for such studies and has thus far been shown to provide practical engineering insights (Janssen *et al*. 2013, Mittal *et*

*Corresponding author, Postdoctoral Research Fellow
E-mail: j.townsend@cranfield.ac.uk
[a]Research Assistant
[b]Research Assistant
[c]Research Assistant
[d]Lecturer

al. 2018, van Druenen *et al*. 2019).

In addition to experimentation and CFD simulations, industrial building standards provide further means to evaluate the potential impact of natural winds on loaded areas of buildings. In the present research, two sets of industrial standards are considered that provide analytical solutions for estimating these wind loads. The first standard, originally published in July 1997, is the BS 6399- 2:1997 standard (British Standards Institution 2002). This standard has since been withdrawn and superseded by the current standard, BS EN 1991-1-4:2005 + A1:2010, which is formed of the BS EN 1991-1- 4:2005 standard (British Standards Institution 2010) and the UK National Annex (NA) incorporating National Amendment A1 (British Standards Institution 2005). The current standard forms partof the EN Eurocode series and also represents the current European standard for wind actions on structures.

This research directly compares empirically-derived pressure-distribution values from the old British standard and current European standard with RANS simulations of flow past a hipped roof using a commercial CFD software, ANSYS Fluent. Limited investigations have been performed to-date that seek to directly compare numerically obtained results with industrial building standards. Most notably, Abdelfatah *et al*. (2022) performed experimental and numerical investigations using RANS modeling for an elevated coastal house wherein pressure coefficient data was compared to the United States ASCE 7-16 building standards. However, their focus was not concerned with the predictive capability of different numerical approaches. Within the current literature, Tominaga *et al*. (2008a) demonstrated that the k–ϵ Realizable model performed well according to experimental data in terms of the velocity field predictions. Tominaga and Stathopoulos (2009) have shown that the k–ϵ RNG model offered superiority in predicting turbulent kinetic energy levels surrounding building corners and velocity profiles within wake regions. The k–ϵ RNG and k–ω SST (Shear Stress Transport) have been shown to provide satisfactory predictions in terms of the turbulent kinetic energy fields and velocity profile prediction by Tominaga *et al*. (2015) where an underestimation is found for the k–ω variant. The k–ω Standard model has also been shown result in better predictions for the surface pressure distribution compared to the k–ϵ Realizable model (Ozmen *et al*. 2016). Amini and Memari (2021) compared the surface pressure distribution of k–ϵ Standard, RNG, Realizable, and k–ω SST models finding the k–ϵ Standard to over-predict pressure coefficients at building corners. While disparity exists between these different RANS modeling formulations, it is still relatively unclear how they fare whencompared to industrial building standards. Should CFD be used an engineering analysis tool for future building construction then it is critical to possess knowledge regarding standard practices for the CFD methodology.

Therefore, the present research concerns the interaction of fluid flow, viz. wind, and a building with a hipped-roof design. We aim to provide a systematic comparison in terms of pressure coefficients and wind loading on the structure using data derived from the two industrial buildingstandards and CFD simulations utilizing the popular

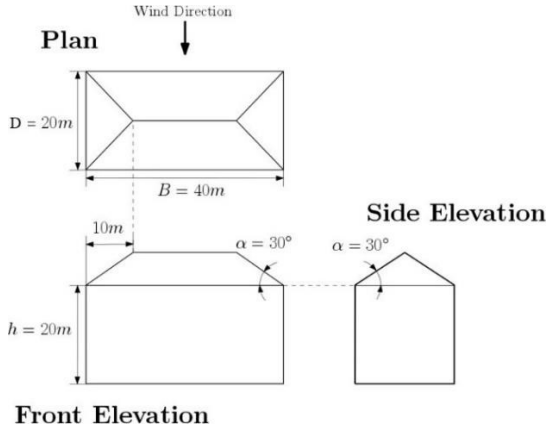

Fig. 1 Building sketch showing the plan, front, and side elevation perspectives used in the present research

turbulence models within the k–ϵ RANS family. Hence, we are able to fathom how well the RANS models perform against these industrial standards and where they deviate in terms of the individual characteristics for an investigation of the flow past the hipped-roof building−the full problem specification is provided within Sec. 2. The remaining structure of this work is as follows: the wind loading pressure-distribution from the old British standard (BS 6399-2:1997) and current European standard (BS EN 1991- 1-4:2005 + A1:2010) are presented in Sec. 3. This is followed by the computational methodology and numerical set up of the CFD simulations in Sec. 4. Finally, qualitative CFD results, along with a comparison of external pressure-distributions from numerical and analytical data is shown in Sec. 5 as well as the extracted pedestrian comfort levels. The CFD data contain results found from using three flavors of k–ϵ RANS turbulence model: the standard, RNG, and Realizable.

2. Problem specification

A 3D geometry representing a simplified closed static apartment building without any external features is shown in Fig. 1. The building has a length B = 40 m, a breadth D = 20 m, and eave height of h = 20 m. The hipped-roof is characterized by a pitch of α = 30° which yields a building height H of 25.77 m. The wind impinges the building normal to the length on one side as shown from the plan view in Fig. 1. The wind speed is chosen to be representativeof conditions in Cranfield in the United Kingdom. Cranfield is located inland, approximately halfway between Oxford and Cambridge, and approximately 80 km north of London. Calculations based on the industrial standards require a fundamental wind speed v_{b0} chosen according to a geographical location. Fig. 6 within British Standards Institution (2002) illustrates basic wind speeds at various locations throughout the United Kingdom from which we note that Cranfield is situated between an isoline of 20 and 21 m/s. The wind speeds provided are typically measured at a height 10 m above ground in open terrain. Therefore, we consider the latter value as a more conservative estimate for

our fundamental basic wind speed such that throughout this work $v_{b0} = 21$ m/s. A committee of regulatory bodies in the UK established a set of empirical relations to calculate wind loading on various sections of common buildings. This initial set of guidelines, the BS 6399- 2:1997 standard (British Standards Institution 2002), has since been replacedwith the Eurocode update, BS EN 1991-1-4:2005 +A1:2010 (British Standards Institution 2010, 2005). Throughout Sec. 3, we present the methodologies accordingto the aforementioned standards for calculating the building pressure distribution from Fig. 1 located in Cranfield, UK.

3. Analytical solutions

3.1 Solution based on BS 6399-2 (Old system numerical)

The building used in this investigation is considered to be an apartment building with masonry walls. Therefore, the 'building-type factor' k_b according to Table 1 in British Standards Institution (2002) is $k_b = 0.5$. Using the parameters H and k_b we can establish whether the current building arrangement falls within the BS 6399-2:1997 standard remit. This standard allows for a critical dynamic augmentation factor of $C_r < 0.25$ and height $H < 120$m. Using Fig. 3 in British Standards Institution (2002) which illustrates the limit of applicability of the standard in terms of the building height H, the building-type factor k_b, andthe critical dynamic augmentation factor of C_r , we conclude that the standard is applicable for the current study.

3.1.1 Standard wind speeds

The basic wind speed, as justified in Sec. 2, is given as $v_{b0} = 21$ m/s. In addition, a site wind speed v_s must be calculated which considers additional parameters pertaining to the altitude, wind direction, seasonal factors, and a probability factor. These parameters are as follows:

An altitude factor S_a, which is used to adjust v_{b0} for the altitude of the site above sea level, is dependent on the problem-specific topography. The altitude factor S_a is found from,

$$S_a = 1 + 0.001\delta s \tag{1}$$

where δs denotes the site altitude (meters above sea level) which for Cranfield Airport is $\delta s = 109$ m. Therefore, the altitude factor is computed to be $S_a = 1.109$.

A direction factor S_d is used to adjust v_{b0} to produce wind speeds with the same risk of being exceeded in any direction. Since the orientation of the building is arbitrary, we take the most conservative value of $S_d = 1$.

A seasonal factor S_s can be used to account for specific sub-annual periods which is critical for temporary buildings. For permanent buildings, such as in the present case, the seasonal factor can be taken as $S_s = 1$.

A probability factor S_p can be used to adjust v_{b0} accounting for an annual risk of the hourly mean windspeed being exceeded by what is considered as typical. For normal building applications, this value is not exceeded

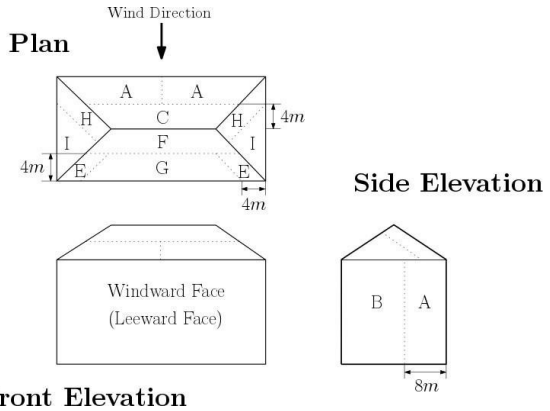

Fig. 2 Building sketch showing the surfaces defined under the BS 6399-2:1997 standard used to determine the external pressure coefficients c_{pe}

hence we use a probability factor of $S_p = 1$.

Using the above parameters, the site wind speed can be computed according to,

$$v_s = S_a S_d S_s v_{b0}, \tag{2}$$

which yields a site wind speed of,

$$v_s = 23.289\text{m/s}. \tag{3}$$

Finally, the effective wind speed v_e requires a terrain and building factor S_b for its calculation. This factor considers the effective height of the building (calculated earlier to be 25.77m), the wind effect of distance of the building from the sea, and whether the building is in a town or country terrain. Using Table 4 in British Standards Institution (2002) and considering the fact that Cranfieldsite is located more than 100 km from the sea, the terrain and building factor is given as $S_a = 1.8161$. The effective wind speed is then found to be,

$$v_e = S_b v_s = 42.295 \text{ m/s}. \tag{4}$$

3.1.2 Dynamic pressure

The effective wind speed v_e is then used to compute the dynamic pressure q_s given by

$$q_s = \frac{1}{2}\rho v_e^2, \tag{5}$$

where ρ is the fluid density. This gives rise to a dynamic pressure of

$$q_s = 1096.6 \text{ Pa}. \tag{6}$$

3.1.3 Pressure coefficients and loads

External and internal pressure coefficients for the walls and roof are required, denoted by c_{pe} and c_{pi} respectively. They enable, alongside the dynamic pressure, a calculation of the loading for each area section of the building.

Fig. 2 shows the surface subdivision proposed under the BS 6399-2:1997 standard. To establish these divisions a scaling length b must be computed according to the minimum of the crosswind breadth of the building B and twice the building height 2 H. From Fig. 1, B = 40 m

Table 1 External pressure coefficients, external pressure, and wind loads according to the BS 6399-2:1997 standard

Surface		a (m)	$A\ (m^2)$	c_{pe}	C_{ae}	$p_e\ (Pa)$	$p\ (Pa)$	$F(kN)$
Windward		44.72	800	0.85	0.83	773.65	1001.23	805.78
Leeward		44.72	800	-0.5	0.83	-455.09	-221.51	-177.21
Sides	A	21.54	160	-1.3	0.89	-1268.77	-1035.19	-165.63
	B	23.22	240	-0.8	0.88	-772	-538.42	-129.22
Roof	A	20.52	83.14	-0.5	0.9	-493.73	-727.05	-60.45
	C	26.91	180.13	-0.2	0.87	-190.81	-424.39	-76.45
	E	12.17	27.71	-1.3	0.93	-1325.79	-1092.21	-30.27
	F	24.44	110.82	-0.8	0.88	-772	-538.42	-59.68
	G	26.91	180.13	-0.6	0.87	-572.43	-338.85	-61.04
	H	15.14	41.57	0	0.92	0	233.58	9.71
	I	16	73.9	0	0.92	0	233.58	17.26

and $2H = 51.54$ m, hence the scaling length is found to be $b = 40$ m. Noting that for the windward and leeward building faces $D/H < 1$, and the fact that we consider an isolated building such that any funneling effects can be neglected, we are permitted to use the values of c_{pe} given in Table 5 of British Standards Institution (2002). In addition, we require a size factor C_a which, in reference to Fig. 4 from British Standards Institution (2002), can be determined using the diagonal length a and area of each division in Fig. 2. These values along with the external pressure coefficients are displayed in Table 1.

Upon computing C_a we may determine the external pressure acting on the building p_e on each building subdivision using the relationship,

$$p_e = c_{pe} C_{ae} q_s. \tag{7}$$

The BS 6399-2:1997 standard requires the calculation of the internal pressure coefficient c_{pi} to counteract the exterior pressure. We consider the case where the internal doors are much more permeable than the main doors and windows of the building and the external walls are all equally permeable. The internal pressure can be found from,

$$p_i = c_{pi} C_{ai} q_s. \tag{8}$$

Thus, according to Table 16 of British Standards Institution (2002), we may assume the internal coefficient is constant for all surfaces of the building and that $c_{pi} = -0.3$. To complete the calculation of C_{ai} a reference diagonal length is required which is found from,

$$a_i = 10\sqrt{A}, \tag{9}$$

in Fig. 2. We then obtain a reference diagonal length of $a_i = 261.71$ m. Therefore, using this value of a_i with Fig. 4 in British Standards Institution (2002), we find $C_{ai} = 0.71$. From Eq. (8) we find the internal pressure to be,

$$p_i = -233.58, \tag{10}$$

It is now possible to compute the pressure $p = p_e - p_i$ and the loading $F = pA$ on each surface area. These values have been calculated and are displayed in Table 1. Using Table 1 the net horizontal force F can be calculated as,

$$F = F_{WW} + F_{LW} + 2F_{A,Roof} + F_C + 2F_E + F_F + F_G, \tag{11}$$

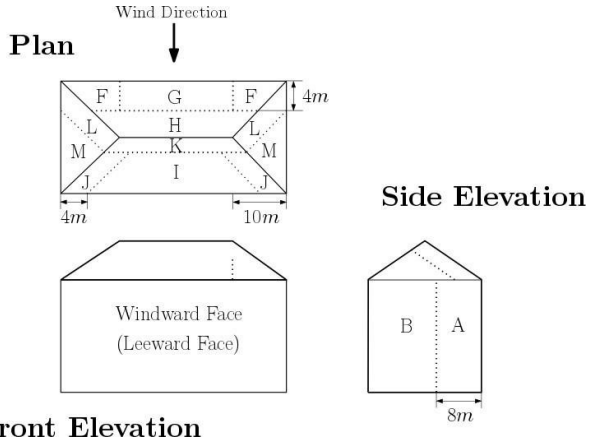

Fig. 3 Building sketch showing the surfaces defined under the BS EN 1991-1-4:2005 + A1:2010 standard used to determine the external pressure coefficients c_{pe}

which yields a net horizontal force,

$$F = 249.96\text{kN}. \tag{12}$$

3.2 Solution based on BS EN 1991-1-4:2005 + A1:2010 (Current System)

According to Sec. 1 of British Standards Institution (2010), the Eurocode is applicable for the design of buildings with a height less than 200 m. In the present research, the building height is computed to be $H = 25.77$ m hence, the Eurocode standard equally applies.

3.2.1 Basic Wind Velocity

The basic wind velocity v_b is defined in Sec. 4.2 of British Standards Institution (2010) as,

$$v_b = c_{dir} c_{season} v_{b0}, \tag{13}$$

where v_{b0} is the fundamental basic wind speed, c_{dir} is the directional factor and c_{season} is the seasonal factor. Following the same reasoning as previously used for the BS 6399-2:1997 standard, the conservative values for the seasonal and directional factor of unity may be used. Therefore, the basic wind speed is, again, given as $v_b =$ 23.289 m/s at a height of 10 m above open terrain.

Table 2 External pressure coefficients, external pressure and wind loads according to the BS EN 1991-1-4:2005+ A1:2010 standard

Surface		Intact	DI	D2	Intact	DI
Windward		800	0.752	724.48	1013.68	810.94
Leeward		800	-0.404	-389.21	-100.01	-80
Sides	A	160	-1.2	-1156.08	-866.88	-138.7
	B	240	-0.8	-770.72	-481.52	-115.56
	F	36.95	-0.5	-481.7	-779.72	-28.81
	G	92.38	-0.5	-481.7	-779.72	-72.03
Roof	H	180.13	-0.2	-192.68	-490.7	-88.39
	I	175.51	-0.6	-578.04	-288.84	-50.69
	J	36.95	-1.3	-1252.42	-963.22	-35.59
	K	27.71	-0.8	-770.72	-481.52	-13.34
	L	41.57	0	0	289.02	12.01
	M	73.9	0	0	289.02	21.36

3.2.2 Peak velocity pressure

Calculation of the peak velocity pressure q_s is described in British Standards Institution (2010) through an expression that considers the mean wind velocity, the turbulence intensity, and a reference height. However, the UK National Annex (British Standards Institution 2005) recommends a different formulation, inherited from the old standard (British Standards Institution 2002) - this is because the Eurocode refers to the National Annex whenever a particular magnitude is more suitable for a certain country. Since orography is not a factor, expression NA.3b in British Standards Institution (2005) is considered and an exposure factor of $c_e = 2.9$ is extracted from Fig. NA.7 in British Standards Institution (2005). Therefore, the peak velocity pressure is found to be,

$$q_p = 963.4\text{Pa}. \tag{14}$$

3.2.3 Pressure coefficients and loads

The values of c_{pe} chosen are those given in Tables NA.4 and NA.8 from British Standards Institution (2005) since the National Annex varies from the Eurocode coefficients for adaptation to the British environment. We consider a value of $h/D = 0.644$ for use of Table NA.4 in British Standards Institution (2005) and note that the building does not contain a surface area greater than 10 m^2, hence only values of $c_{pe,10}$ will be used. The external pressure may be calculated using,

$$p_e = c_{pe} q_p. \tag{15}$$

The internal pressure, on the other hand, is calculated in British Standards Institution (2010) as a function of the open areas in the wall. As this information is not available for this case we used the value suggested by the Eurocode of $c_{pi} = -0.3$. Therefore,

$$p_i = c_{pi} q_p = -289.02\text{Pa}. \tag{16}$$

To calculate the wind loading over each building subdivision a structural factor $c_s c_d$ requires computation. As we expect the building walls to be structured and exhibit negligible dynamic behavior, the conservative value of $c_s c_d = 1$ is chosen. Thus, the wind loading F is found from,

$$F = (c_s c_d p_e - p_i)A = pA. \tag{17}$$

In a similar manner to the BS 6399-2:1997 standard, we can compute the pressure coefficients and wind loading on each surface subdivisions shown in Fig. 3 as defined by the Eurocode (British Standards Institution 2010). The pressure coefficients and wind loading on each building sub-surface are presented in Table 2. From Table 2, we find the net horizontal force F from,

$$F = F_{WW} + F_{LW} + 2F_F + F_G + F_H + F_I + 2F_J + F_K, \tag{18}$$

resulting in,

$$F = 377.69\text{kN}. \tag{19}$$

Table 3 Flow conditions from which the first layer of cell thickness was calculated

Parameter	Value
Flow Velocity, V (m/s)	23.29
Density, ρ (kg/m^3)	1.25
Viscosity, μ (kg/ms)	1.84×10^{-5}
Reynolds Number, Re	3.17×10^{7}
Non-dimensional Wall Distance, y^+	50
First Layer Thickness, Δs (m)	9.5×10^{-4}

Table 4 Details of the generated grid, indicating the box edge size within the density box option from Pointwise

Level	Edge Size			Number of
	Model	Box	Domain	Elements
Coarse	0.3	3.00	6	2,214,246
Medium	0.3	1.50	6	2,640,433
Fine	0.3	0.75	6	5,127,027

4. Computational set up

Throughout Sec. 4 we describe the CFD methodology used to evaluate the impinging wind on a building located in Cranfield, UK, as presented in Sec. 2. For the grid generation and numerical simulations, we employ the commercial software Pointwise V18.3 R2 and ANSYS Fluent 19.1, respectively

4.1 Grid generation

The computational grids for this investigation are designed through consideration of the likely regions that would contain flow structures of interest such as re-circulation regions and horseshoe vortices that are typical of fluid flow around obstacles resembling buildings (Martinuzzi and Tropea 1993). The grids were generated for compatibility with the k–ϵ RANS turbulence models. The first boundary layer cell height Δs surrounding the building was based on a non-dimensional wall distance of $y^+ = 50$. This ensured that the y^+ remained within the best practice

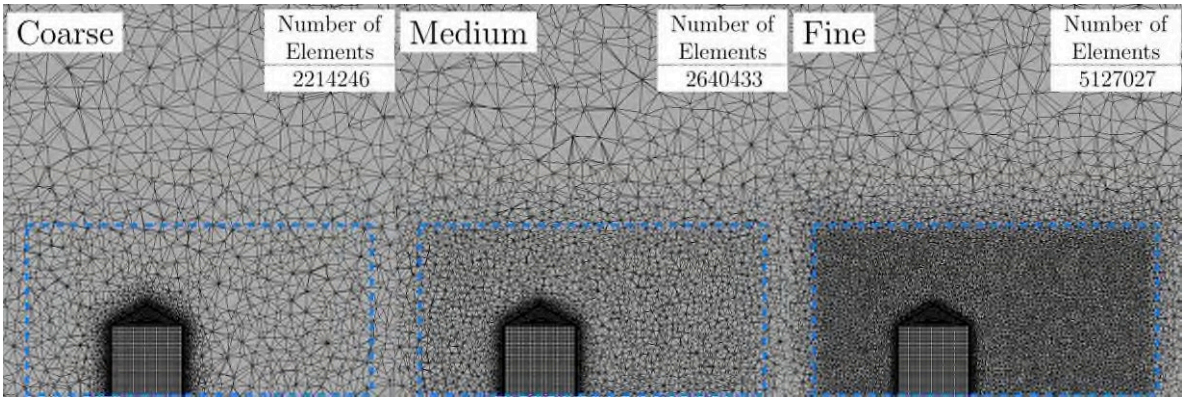

Fig. 4 Grids generated for the grid convergence study in which the refinement region surrounding the building can be see within the blue box

guidelines for this model, whereby one should consider $30 < y^+ < 300$. Pointwise was used to create the mesh whereby the T-Rex (anisotropic tetrahedral extrusion)algorithm was responsible for generating the viscous off- wall layers Steinbrenner and Abelanet (2007). A total of 30 layers were created with a growth-rate of 20% that surrounded the model only and not the ground region — this simplifies the grid generation procedure and reduce computational cost. The conditions used to compute the firstlayer of thickness Δs are found in Table 3. Standard wall functions were employed for all RANS models considered in the present work.

As part of the verification procedure required to increase confidence in the simulated data, a grid convergence study is performed. The grids were refined within set boundaries in the computational domain such that the outer regions of the domain that have little influence on the solution remain unchanged. The refinement region itself was chosen based on insights gained from the literature. Through the experiments performed by Martinuzzi and Tropea (1993), it was found that for obstacles with a width-to-height ratio of 2-which is similar to the geometry considered in the present work-that the separation point ahead of the model was almost equal to the height of the model whilst the rear re- attachment point was 2.5 times the height. Based on these considerations, the refinement region is chosen such that it extends one model height from the side and highest point ofthe geometry. We consider the model height without the roof hence the model height for this scenario was taken to be 20 m.

Three grids were generated for the grid convergence study, a coarse, medium, and fine configuration which are displayed in Fig. 4. The grid refinement was performed within the specified refinement region, shown as a blue box, and the remainder of the computational domain was left unchanged. Details of the three grids are provided in Table 4 which specifies the changes to the refinement region and the corresponding number of elements this change entails. Fig. 5 presents a more detailed visualization of the finest grid generated. The extruded viscous layers are shown where it can be seen that these layers are orthogonal to the model and grow in a consistent manner. Finally, we note that the size of the entire computational domain is 420 m × 320 m × 120 m (L × W × H) and the refinement box is 90 m × 80 m × 45 m.

4.2 Boundary conditions

The atmospheric boundary layer (ABL) represents the lowest part of the troposphere that is directly influenced by the Earth's surface and responds to surface forcing with a timescale of approximately one hour or less (Stull 1988). Two computational challenges are associated with modeling the ABL. Firstly, resolving the entire height of the ABL would require a computational domain far larger than the dimensions of any building in question, which may result in an impractical computational expense. Secondly, surface features are difficult to model, hence they are often excluded from ABL implementations and instead one may opt to use a roughness factor to account for an in-homogeneous surface (Liu *et al*. 2018).

Early work considering the use of k–ϵ RANS turbulence models for ABL simulation is performed by Richards and Hoxey (1993). It was suggested that boundary conditions used should be able to generate the ABL in the absence of any flow obstacle and that a constant shear stress should be applied to the top of the domain in the flow direction. It has been demonstrated that a no-slip boundary condition at the ground level will fail to sustain an acceptable ABL (Hargreaves and Wright 2007) which led to a proposed solution that involved replacing the standard k–ϵ model with a bespoke version that included a modified law-of-the- wall to correspond with that of the ABL, they also applieda shear stress to the top layer of the domain. Other computational studies with the aim of re-producing a stable ABL have adopted a different approach such as using a modified turbulent kinetic energy transport equation to initialize the flow at the inlet and to calculate the dissipationrate (Yang *et al*. 2009). The data presented therein shows a decay in turbulent kinetic energy with height, which was, as expected, in contrast to what was found by Richards and Hoxey (1993). Research has found that it is essential for the inlet conditions, the turbulence model, the ground, and the top of the domain to form a consistent set to ensure that the specified flow is intended rather than unintended (Richards and Norris 2011). From the data presented by Juretić and

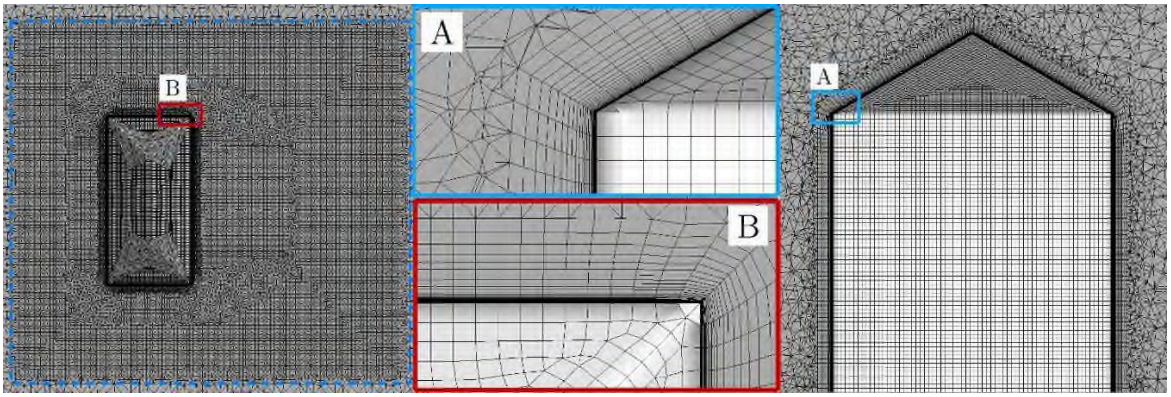

Fig. 5 A detailed view of the finest grid generated. Highlighted zone A displays the viscous layers growing from the model at the edge between the wall and the roof. Zone B displays the edges at the base of the model in which the T-Rex elements originate from

Kozmar (2013), it can be observed that the *k–ϵ* turbulence model is capable of modeling decreasing turbulence parameters with height as discussed by Yang *et al*. (2009).

An appropriate inlet boundary condition is required to sufficiently model the ABL profile. The boundary condition at the inlet for the mean velocity, turbulent kineticenergy, and the turbulence dissipation rate are taken from Crasto (2007) where they were successfully applied within the commercial software ANSYS Fluent for the simulation of ABL-related problems. The equations for the velocity, kinetic energy, and turbulence dissipation rate are respectively given by,

$$U(y) = \frac{u_r}{\kappa} \ln\left(\frac{z}{z_0}\right), \tag{20a}$$

$$k(y) = \frac{u_r^2}{\sqrt{C_\mu}}\left[1 - \frac{z}{z_h}\right]^2, \tag{20b}$$

$$\epsilon(y) = \frac{1}{\kappa}\frac{u_r^3}{z}. \tag{20c}$$

where $z_0 = 0.03$ m is the roughness length for a village target terrain, z_h is the roughness height of the ABL, C_μ is a k–ϵ model constant specified by the default value of the software as 0.42 , κ denotes the turbulent kinetic energy (TKE), and u_c corresponds to the friction velocity whichis calculated based on the previously obtained basic wind speed at a height of 10 m above open terrain. The velocity equation is a log-law equation whilst the equations of TKE and turbulence dissipation rate match the velocity condition and are properly reduced throughout to the free-stream
flow. The ABL velocity profile measured at the inlet of the computational domain for the present study is shown in Fig. 6.

The outlet of the computational domain is set to be an outflow type boundary condition as no information is provided regarding the flow at the outlet, hence all gradients are set to zero with the exception of the pressure field. The top and sides of the domain are prescribed the symmetry boundary condition to negate their effect on the flow and essentially simulate an infinitely large domain resembling real-world conditions. The expressions in Eq. (20) were used to directly produce a highly resolved inlet profile consisting

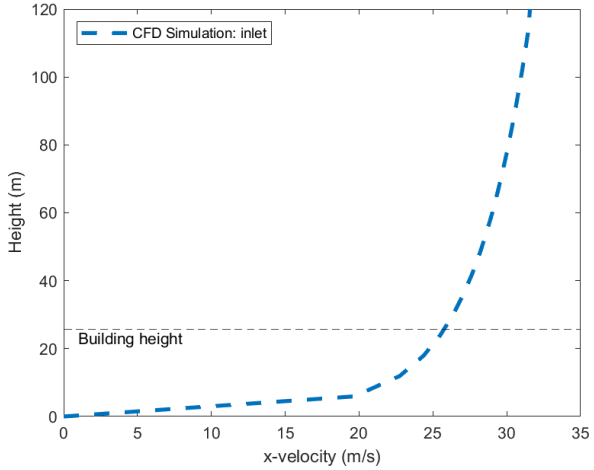

Fig. 6 Building sketch showing the surfaces defined under the BS EN 1991-1-4:2005 + A1:2010 standard used to determine the external pressure coefficients c_{pe}

of 240 data points. This was incorporated into ANSYS Fluent 19.1 through the user defined function (UDF) feature and linked to the inlet boundary condition. The model itself and the ground of the domain were assigned the wall (no-slip) boundary condition.

4.3 Numerical methodology

The numerical simulations presented in this work are all performed using the commercial software package ANSYS Fluent 19.1 using the pressure-based solver. Transient simulations are performed after initial steady-state simulations revealed time-dependent behavior which hindered any possible convergence of the residuals, henceall results presented in this work are achieved using a time-dependent formulation of the incompressible Navier–Stokes equations. A total simulation time of 120 seconds with a time-step size $\Delta t = 0.06$ s is used based on extensive numerical testing which is deemed sufficient to capture all flow features and consistently converges within 20 iterations per time- step with a convergence criterion for all flow variables set to 10^{-4}. Within the elapsed simulation

Table 5 Flow conditions from which the first layer of cell thickness was calculated

Parameter	Scheme/Value
Pressure-Velocity Coupling	SIMPLE
Gradient	Least Squares Cell-Based
Pressure	PRESTO!
Momentum	2nd Order Upwind
Turbulent Kinetic Energy	2nd Order Upwind / Power Law*
Turbulent Dissipation Rate	2nd Order Upwind / Power Law*
Time Integration	Bounded 2nd Order Implicit
Frozen Flux Formulation	Activated
High-Order Term Relaxation	Activated
Time-Step Size Δt	0.06s
Iterations Within Time-Step	30
Total Number of Iterations	2000
Total Simulation Time	120s
Flow Statistics Recorded for	All

* Used for the k–ϵ Realizable model only.

Table 6 The three grid resolutions and corresponding time-averaged drag coefficients for the k–ϵ Standard, RNG, and Realizable turbulence models

Grid Level	Number of Elements	$C_{D,\text{Standard}}$	$C_{D,\text{RNG}}$	$C_{D,\text{Realizable}}$
Coarse	2,241,246	0.6212	0.6337	0.5867
Medium	2,640,433	0.6394	0.6534	0.6101
Fine	5,127,027	0.6231	0.6643	0.6201

Table 7 GCI results alongside their corresponding k–ϵ turbulence models as well as the order of convergence P and the range denoting the resemblance of the results with the asymptotic range

Model	P	GCI Fine, Medium	GCI Medium, Coarse	Range
standard	3.17	2.57%	13.92%	0.1535
RNG	2.10	2.78%	23.02%	0.1038
Realizable	2.38	2.33%	25.58%	0.0791

time this also allows for the flow to complete six passes through the domain.

For all simulations the SIMPLE (Semi-Implicit Method for Pressure Linked Equations) algorithm is used to couple the pressure and velocity. This method is computationally expensive since it corrects the pressure predictions in multiple iterations prior to updating the solution in time, as well as requiring the storage of multiple grids, both the original and staggered. Despite this, the algorithm is robust and proved stable for the current study. The PRESTO! (PREssure STaggering Option) scheme is used as a means of pressure discretization which again provided a stable and robust solution when compared to the other schemes available. The PRESTO! scheme increases the computational cost which is associated with the fact that it requires the storage of values from another staggered grid arrangement.

In all cases the momentum is discretized using a second-order accurate scheme. The turbulent kinetic energy and energy dissipation rate are discretized with second-order accuracy for both the k–ϵ Standard and RNG models

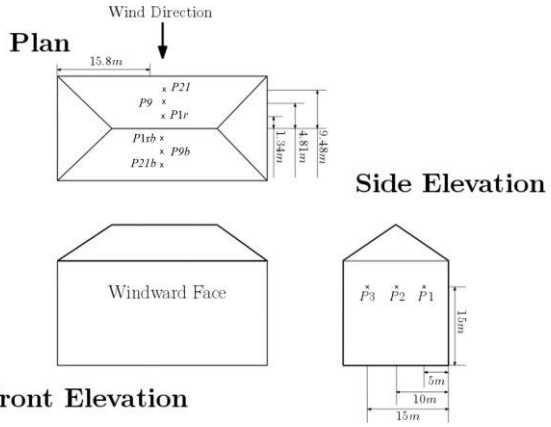

Fig. 7 Locations of pressure probes used for the CFD and industrial standards comparative study

whereas for the k–ϵ Realizable model a power law was used for its discretization. The high-order term relaxation (HOTR) option was switched on to aid in stabilizing the solution as well as the frozen flux formulation, which essentially linearizes a portion of the convective flux and solves it through the mass flux at the cell interface from the previous time-step. Although the order of accuracy is intact,the non-linearity of the solution is sacrificed to improve the convergence of the solution. This does not affect the accuracy of the solution which is initialized with highly accurate conditions and achieved due to the initial ABL information provided. The bounded second- order implicit method is employed for the time integration for which a user-defined input of the Courant number is not required. Finally, Table 5 provides a summary of the numerical methods and software options chosen for the current investigation.

5. Results

5.1 Grid Convergence Study

A grid convergence study is performed as a means of verification for the forthcoming results. In particular, we compute the Grid Convergence Index (GCI) which enables us to quantify the effect of an increasing grid resolution (Roache 2009). A GCI measures the percentage that the computed value is away from the asymptotic numerical value and therefore how much the solution would change with a further grid refinement (Oberkampf and Trucano2002). The GCI is computed using three grid resolutions, refined in the appropriate region as discussed in Sec. 4.1, and a calculation of the time-averaged drag coefficient C_D
is employed as a parameter for measuring the GCI itself.

The grid convergence study was performed for each flavor of the k–ϵ turbulence model using three levels of grid resolution. The time-averaged drag coefficients are presented in Table 6. With the exception of the k–ϵ Standard model, the RNG and Realizable model display an increasing value of C_D as the grid is refined. The GCI results demonstrate behavior similar to what is expected from a continuous flow problem however due to the inherent non-

Table 8 Discrete data of the external pressure coefficients c_{pe} founds from the building standards BS 6399- 2:1997 and BS EN 1991-1-4:2005 + A1:20101, and time-averaged CFD results

Case	Roof						Side		
	$P1r$	$P9$	$P21$	$P1rb$	$P9b$	$P21b$	$P1$	$P2$	$P3$
BS 6399-2:1997	−0.2	−0.2	−0.5	−0.8	−0.6	−0.6	−1.3	0.8	−0.8
BS EN 1991-1-4:2005	−0.2	−0.2	−0.5	−0.8	−0.6	−0.6	−1.2	−0.8	−0.8
Realizable	−0.12	−0.09	−0.13	−0.081	−0.065	−0.069	−0.17	−0.2	−2.2
Standard	−0.153	−0.04	−0.21	−0.11	−0.084	−0.09	−0.15	−0.18	−0.2
RNG	−0.09	0.12	−0.079	−0.06	−0.067	−0.08	−0.15	−0.18	−0.17

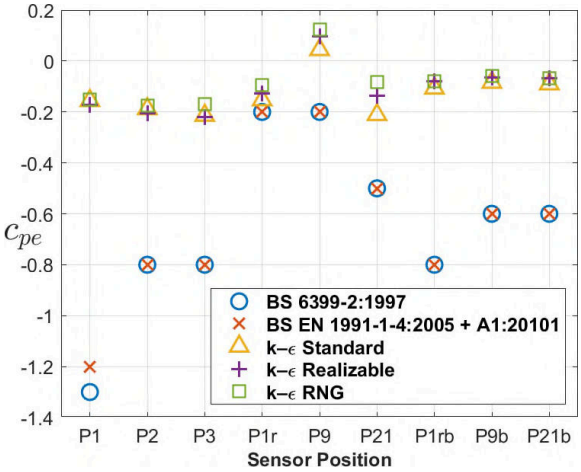

Fig. 8 Graphical comparisons of external pressure coeffici ents c_{pe} founds from the building standards BS 6399 and BS EN 1991, and time-averaged CFD results

linearity in the solution, the refinement of the grid still leads to a result far from the asymptotic range which is indicated in Table 7 as "Range". The computed order of convergence P agrees with the theoretical order chosen for this study through the second-order discretization strategy. The final GCI values when the resolution was increased from the medium to fine grid yields a GCI below 3% which we deem acceptable for the current study. Therefore, in the interest of computation expense and accuracy, all future numerical simulations are performed using the medium grid resolution.

5.2 Comparison of CFD and industrial standards

Comparisons between the external pressure coefficient c_{pe} are made for the five available data sets: three resulting from the CFD simulations for each flavor of the k–ϵ RANS model and the two analytical calculations based on the BS 6399-2:1997 standard and the Eurocode update, the BS EN 1991-1-4:2005 + A1:2010 standard. The locations of the pressure coefficient measurements are shown in Fig. 7 which are taken at nine locations on the building: three on the windward roof section, three on the leeward roof section,and two along the side of the building. These direct comparisons between simulated and analytical methods are displayed in Fig. 8, with the discrete data also reported in Table 8. An almost identical agreement is found between the two industrial standards. This similarity can be justified by considering the fact that the Eurocode refers to the

Table 9 L_1, L_2, and L_∞ error norms of the external pressure coefficients for the CFD predictions and industrial standards. Values are computed using the pressure coefficient values in Table

	BS 6399-2:1997			BS EN 1991-1-4:2005		
	Realizable	Standard	RNG	Realizable	Standard	RNG
L_1	0.54	0.52	0.56	0.52	0.51	0.55
L_2	0.60	0.59	0.62	0.58	0.57	0.60
L_∞	0.83	0.82	0.86	0.83	0.81	0.86

Table 10 Net Horizontal wind load for the building standards BS 6399-2:1997 and BS EN 1991-1-4:2005 + A1:2010, and time-averaged CFD results

	Net Horizontal P (kN)
BS 6399-2:1997	249.96
BS EN 1991-1-4:2005	377.69
Realizable	288.05
Standard	278.01
RNG	328.72

Table 11 Percentage error for wind loading CFD predictions and industrial standards. Values are computed using the net horizontal wind load values in Table 10

	BS 6399-2:1997			BS EN 1991-1-4:2005		
	Realizable	Standard	RNG	Realizable	Standard	RNG
Error, %	15.24	11.22	31.51	23.73	26.40	13.00

British National Annex for these values, hence the BS EN 1991-1-4:2005 + A1:20101 is based on the BS 6399-2:1997 for this case. It is apparent from Fig. 8 that the numerical results over-predict the solutions based on the industrial standards. This effect is more prevalent for the sides and leeward roof section of the building. The CFD simulations capture greater detail surrounding the leeward side of the building, this analysis indicates that the flow velocity in this region has likely been over-predicted by the industrial standards and in reality, some flow remains attached and is accelerated down the leeward side. Similarly, at the point P9 on the windward side of the roof, we see that flow is accelerated through this section with respect to the freestream velocity and the pressure inadvertently drops. An improved agreement is found on the roof sections for the pressure coefficient, in which the k–ϵ standard model reproduces values more consistent with the standards.

Table 9 lists the L_1 (mean absolute error), L_2 (least-squares error), and L_∞ (maximum error) error norms for the

pressure coefficient values in Table 8 such that we can directly quantify the performance of the k–ϵ RANS models with respect to the industrial standards. It is clear that for both standards, the k–ϵ Standard model predicts these coefficients with the greatest accuracy whilst the k–ϵ RNG model consistently demonstrates the lowest accuracy.

Table 10 reports the net horizontal wind loading for the two industrial standards and available CFD data sets — the CFD results are time-averaged over the simulation run. The BS EN 1991-1- 4:2005 + A1:20101 standard provides a more conservative estimate of the wind loading compared to the older standard and CFD data. From Table 11, it can be seen that the k–ϵ RNG model found the best agreement with the current industrial standard, under-predicting the net horizontal wind loading by less than 15% whereas the k–ϵ standard model under-predicted the current standard by more than 25%. Regarding the outdated standard, the opposite result is obtained, largely because the current standard yields a more conservative estimation of the wind loads such that this prediction is increased by approximately 50%. Therefore, based on the results obtained in this study, the k–ϵ RNG model is recommended for wind loading predictions under the current BS EN 1991-1-4:2005 + A1:2010 industrial standard.

5.3 Flow Analysis

Two CFD post-processing techniques are utilized to qualitatively analyze the captured flow physics of each k–ϵ RANS model. The surface shear stream-traces are presented in Sec. 5.3.1 for the entire building geometry as well as the developed flow behind the building. To further visualize the flow complexity and highlight any predictive differences found between the three flavors of k–ϵ models, we report the ISO surfaces of the Q-criterion in Sec. 5.3.2 which provides insight into the locations where vorticalmotion is present.

5.3.1 Shear surface stream-traces

The predicted wind flow for each k–ϵ model is analyzed in a manner inspired by similar studies for automotive CFD investigations through use of surface shear stream-traces (Krajnović and Davidson 2005). The surface shear stream-traces are visualized across the entire building geometry including the region immediately behind the building where the unstable vortex shedding phenomenon occurs. We note that the unstable flow patterns present a high-degree of associated randomness hence the comparison is performed using time-averaged results over a period of 120 seconds of elapsed flow-time.

Fig. 9 displays the shear surface stream-traces (from top to bottom): at the front, right-hand- side, rear, and roof of the building geometry from results achieved using the k–ϵ Standard (left), k–ϵ RNG (center), and k–ϵ Realizable (right) turbulence models. As a key to understanding the results presented in Fig. 9, we define the following abbreviations.

PBL: Positive Bifurcation Lines
SF: Stable Focus
SP: Saddle Point
NBL: Negative Bifurcation Lines
UN: Unstable Node
SB: Separation Bubble

The frontal building surface displayed in the first row of Fig. 9 shows little difference in the flow predictions given by the three flavors of k–ϵ turbulence model. The unstable node (UN) is the point from which the flow streams emanate and separate into groups either towards the ground which can form a re-circulation region ahead of the building, towards the top of the building such that flow separation and complex flow features can develop behind the building, or towards the sides where additional vortex structures may form. The k–ϵ Standard model predicts a slightly lower UN location than the remaining k–ϵ turbulence models yet none of the models predict the creation of a separation bubble at the top (roof) section. The flow remains attached to the frontal surfaces which is indicated by the positive bifurcation lines (PBL) emanating from the UN.

The second row of Fig. 9 presents the side view of the building in which the observed flow pat- terns display greater difference between the turbulence models used. The k–ϵ Standard model (left) predicted two separation bubbles, one at each side. These faint separation bubbles were observed through the bifurcation lines emanating and terminating side-by-side. The k–ϵ RNG model (center) appears more conservative in its separation bubble prediction, the model predicted a faint bubble closer to the front section on the upper left corner and another one on thebottom right corner; the flow however remains attached to the side with no separation. The k–ϵ Realizable model displays similar behavior with no separation bubble on the side near the edges but with a large bubble, larger than when$k$–ϵ RNG is used. These flow patterns are better visualized with Fig. 10.

The rear surfaces (3rd row of Fig. 9) provide insight of the flow dynamics after the flow passes the hipped roof. The region of low pressure behind the model pulls in the airflow creating a region of strong reverse flow that impacts the rear surface forming an UN point, from which positive bifurcation lines (PBL) emanate. The differences between all the models are subtle such as the location of the UN and the direction towards which the PBL travel. The delayed Negative Bifurcation Lines (NBL) predicted by the k–ϵ Standard and Realizable models are visible, while none of the models display the stable focus (SF) points created at thesides of the model. An important point to highlight is that the stream of PBL emanating from the respective UN leads to the spirals on the roof surfaces when they meet the flow running on the frontal portion of the model.

Studying the top (plan) views (4th row of Fig. 9), it can be seen that the k–ϵ Standard and Realizable models predicted similar patterns. The location of separation indicated by the negative bifurcation lines (NBL) is predicated slightly after the roof edge, while the RNG model predicted it to be almost immediately. This helps to explain the disparity between RANS model predictions concerning the pressure distribution at location, since the flow separation directly corresponds to the pressure on the roof surface. Also, the behavior of the k–ϵ RNG model seen with the

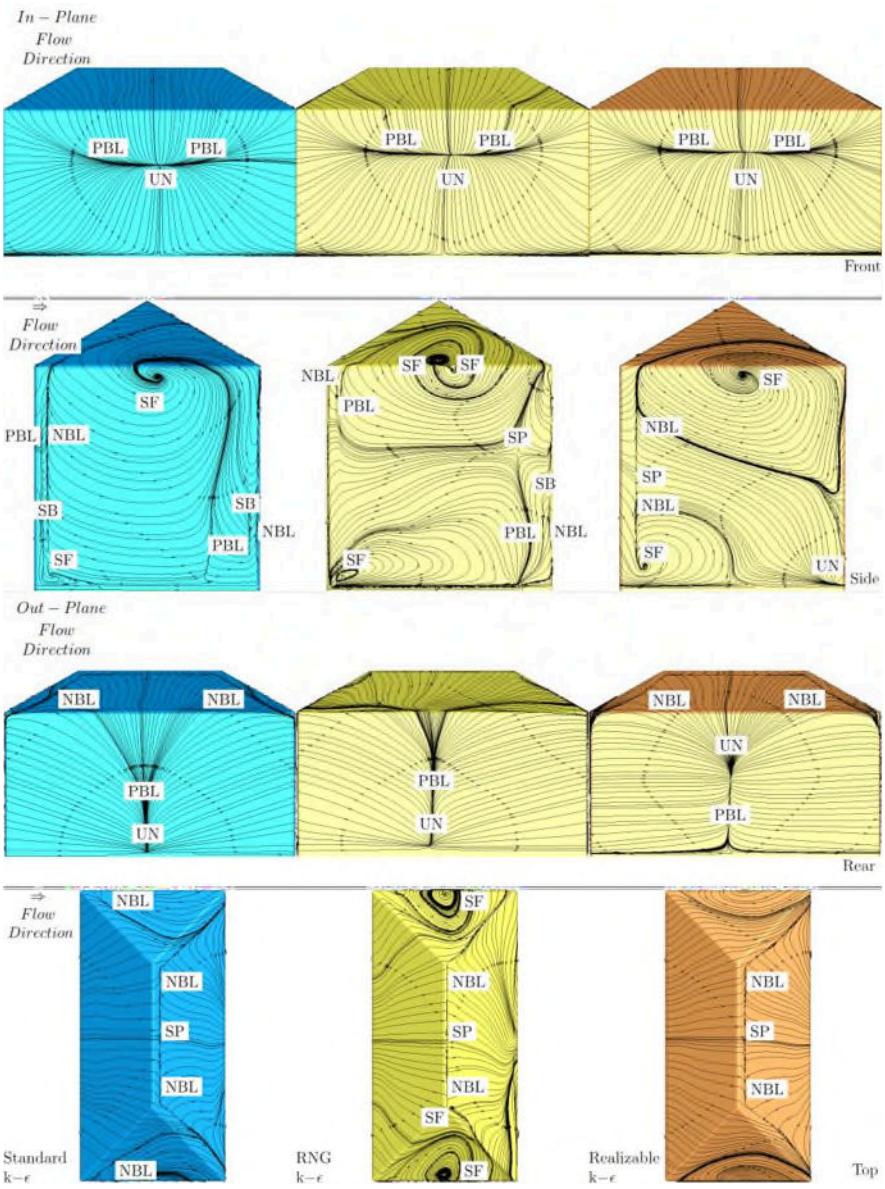

Fig. 9 Shear surface-streams surrounding the building indicating regions of flow separation, re-attachment, flow impact points, and re-circulation regions. The left (blue), center (yellow), and right (orange) buildings correspond to simulation results achieved using the k–ϵ Standard, k–ϵ RNG, and k–ϵ Realizable turbulence models, respectively. From top to bottom we display the building front view, right-hand-side view, rear view, and the plan view

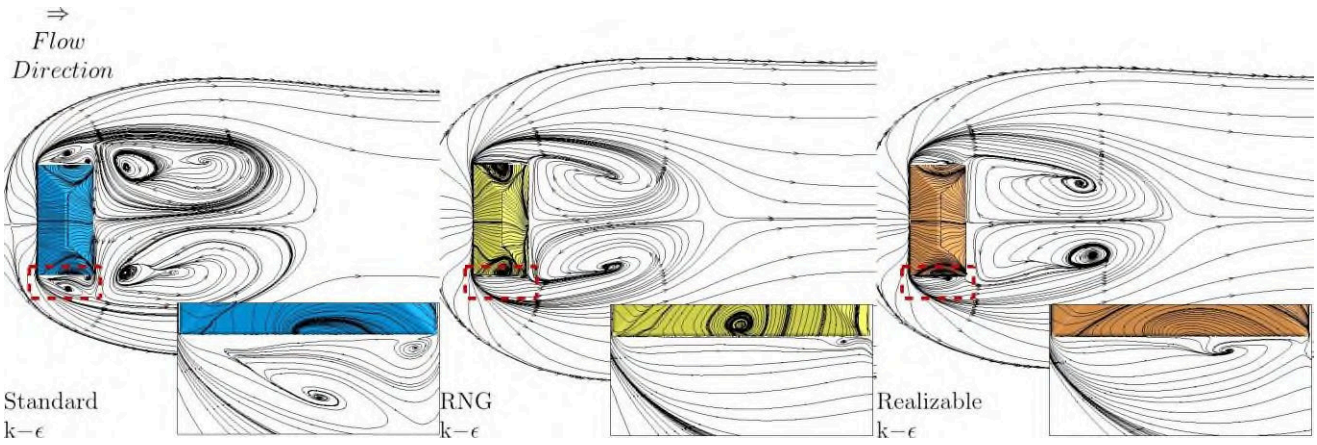

Fig. 10 Top (plan) view of the domain stream-traces for the k–ϵ Standard (left), RNG (center), and Realizable (right) models. This allows for the visualization of the complex flow patterns that develop around and behind the model

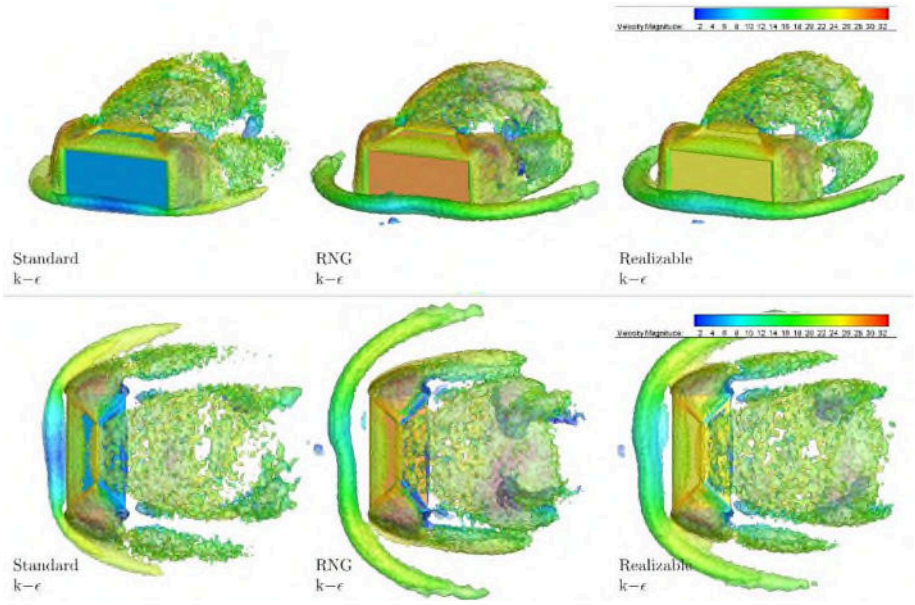

Fig. 11 Q-Criterion ISO surfaces created at levels 0.1, 1, and 10. At the top the isometric view is displayed of the models, while on the bottom, the top (plan) view of the models is provided. This figure serves to illustrate the intensity of separation regions due to the different predictions of each of the models described earlier

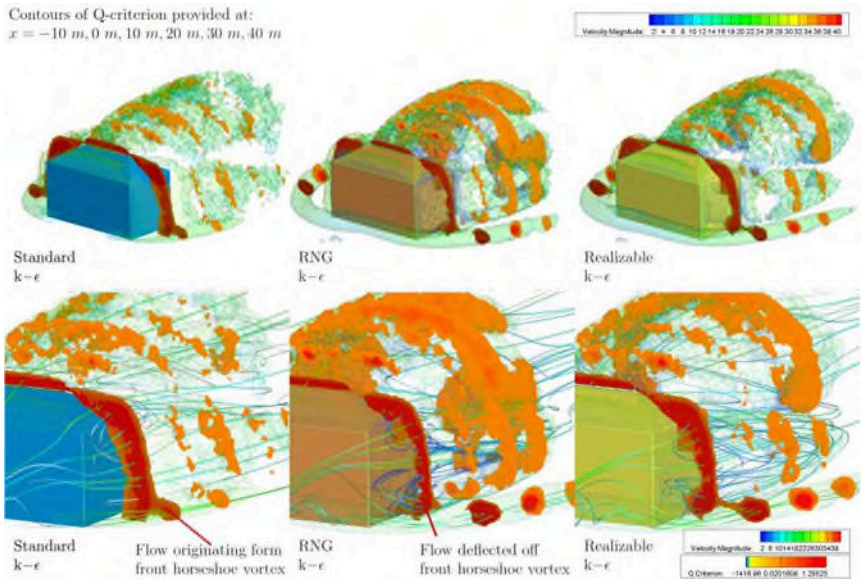

Fig. 12 Transparent Q-criterion ISO surface of value 1 with clipped contours of Q-criterion along with stream ribbons colored by flow velocity magnitude passing through the vortex core regions. This figure presents the origin of the flow responsible for each vortex developed around the model as predicted by each flavor of k–ϵ RANS model

frontal figures discussed earlier develops two large stable focus (SF) points. These SF points are developed upon impact of the advancing flow from the front of the model with the reversing flow off the rear of the model, this is noticed by the traveling NBL on either side of all the turbulence models starting from the SP located at almost themiddle of the roof edge which forces the flow to spiral into the SF points. Another interesting flow feature captured by the RNG model is a faint SF point of the roof of the model appearing on one side only, this flow pattern is expected to have developed on the other side as well given the flow is allowed to be averaged over longer flow passes. Both the k–ϵ Standard and Realizable failed to predict this flow feature due to the delayed separation prediction.

Fig. 10 provides the top (plan) view of the buildings such that we can visualize the complex flow patterns developing around and behind the model. It can be seen that the k–ϵ Standard model predicts larger side vortices as shown through the close-up view. This agrees with the statements made upon studying the side view of the shear streamlines on the model with the two faint separation bubbles and the larger one. The k–ϵ RNG model on the other hand predicted fully attached flow on the largest portion of the side with a small re-circulation region near the corner,

Table 12 Pedestrian comfort criteria

Comfort Level Guideline	Mean Wind Speed Exceeded 5% of the Time	Beaufort Scale	Description
C1+	>10 m/s	>5	Exceeds comfort criteria and not recommended for activities.
C1	10 m/s	5	Acceptable for walking or cycling.
C2	8 m/s	4	Suitable for walking.
C3	6 m/s	3	Appropriate for short-term standing or sitting.
C4	4 m/s	2-3	Appropriate for long-term standing or sitting.

Table 13 Pedestrian comfort and safety criteria for all k–ϵ RANS models

Point	k–ϵ Standard			k–ϵ RNG			k–ϵ Realizable		
	Velocity (m/s)	Comfort Criteria	Safety Criteria	Velocity (m/s)	Comfort Criteria	Safety Criteria	Velocity (m/s)	Comfort Criteria	Safety Criteria
1	1.86	C4	S2	1.48	C4	S2	9.79	C1	S2
2	3.98	C4	S2	5.99	C3	S2	6.73	C2	S2
3	3.13	C4	S2	3.99	C4	S2	5.77	C3	S2
4	3.65	C4	S2	5.53	C3	S2	5.51	C3	S2

whilst the k–ϵ Realizable model predicted a larger vortex yet the flow remains attached to the side for almost half the side length. In the region behind the building, the flow is clearly non-symmetrical for all turbulence models. Also, the extent and strength of the developed vortex depends on the separation developing on the sides of the building, hencethe k–ϵ Standard model produced the largest separation and re-circulation behind the model, followed by the Realizable,and the RNG model.

5.3.2 Q-Criterion visualization

The Q-criterion ISO surfaces produced at levels 0.1, 1, and 10 are shown in Fig. 11. We observe that the models all succeed in predicting the horseshoe vortex ahead of the building, though it is not symmetrical in shape for the results achieved using the k–ϵ RNG and Realizable models. Further investigation of the top (plan) view of the ISO surfaces indicates the effect of earlier flow separation through the wider bubble extending off the sides, it appears atan earlier location for the k–ϵ Standard model, followed by the Realizable, and then the RNG. On the other hand, since the RNG model predicts faster separation on the roof, the separation region on top of the model is much larger and wider than its counterparts, with the standard model predicting the smallest top separation bubble.

Fig. 12 shows a transparent Q-criterion ISO surface of value 1 with clipped contours of Q-criterion along with stream ribbons colored by flow velocity magnitude passing through the vortex core regions. We observe through the velocity ribbons that the flow passing via the horseshoe vortex is actually the flow that was re-circulating ahead of the building in the frontal separation region. Above that we notice that the flow being deflected by this separation region is responsible for the side vortices along with re-circulating flow from the rear separation region. This is the case for both the k–ϵ Standard and RNG models, the Realizable model interestingly predicts that a portion of the frontal recirculating flow is also responsible for the side vortices as displayed through the right section of Fig. 12.

5.4 Pedestrian comfort and safety criteria

Finally, the gathered data is used to compute a comfort index based on one used for a Canary Wharf development project in London. The index is presented in Table 12. It is clear that the C3 and C4 criterion indicate that minimal disturbance is posed to pedestrians and are consequently a desirable building property. Furthermore, for an all-weather safety use (S2 Safety level), the mean wind velocity exceeded once per year has to be less than 15 m/s.

The results for all flavors of k–ϵ RANS model are displayed in Table 13. The wind speeds are extracted through the Tecplot post-processing software as probes where Point 1 corresponds to a location in the center and 3 m away from the building, Point 2 at the center and 3 m behind the building, and Points 3 and 4 are at the center of the sides and 3 m away from the building. All probes are located at a height of 1.5 m above ground level and time- averaged over the 120 s of elapsed flow-time. It can be clearly seen that the standard variant of the k–ϵ model provided the most desirable, almost ideal, pedestriancomfort criterion. The RNG model resulted in slightly less acceptable criterion, however, highly satisfactory nevertheless. The wind speeds generated from the Realizablemodel produced the least satisfactory criterion.

6. Conclusions

In this study, 3D CFD simulations of fluid flow, viz. wind, under environmental conditions representative of Cranfield Village in the UK are performed for a hipped-roof building geometry. The CFD simulations employ three popular variations of the k–ϵ RANS turbulence model: the Standard, Realizable, and RNG. Particular emphasis is placed on calculating the wind pressure and wind loading on the building which is compared to industrial building standards through the BS 6399-2:1997 standard (now obsolete) and the current Eurocode BS EN 1991-1-4:2005 +

A1:20101 standard. Analytical solutions based on the two standards resulted in similar predictions however the current BS EN 1991-1-4:2005 + A1:20101 standard does yield more conservative data. Comparisons with CFD data are made only after a robust grid convergence study is performed wherein convergence of the solution and the minimization of discretization errors with increasing the grid refinement level was found.

CFD data consistently over-predicts the external pressure coefficients compared to the industrial standards. An improved agreement is found on the roof sections for the pressure coefficient, in which the k–ϵ Standard model reproduces values more consistent with the building standards. This analysis indicated that the k–ϵ Standard model was able to more accurately predict the pressure coefficients around the building geometry for both industrial standards however, large disparity between numerical values is not found. In terms of the net horizontal wind loading, the k–ϵ RNG model was unequivocally better-able to replicate the value given by current Eurocode standard since they both yielded the most conservative estimates. Hence, interms of wind loading predication, the k–ϵ RNG model is recommended. Pedestrian comfort and safety criteria are analyzed to complete the study by extracting wind velocity data surrounding the building. It is found that the k–ϵ Standard model predicts the most ideal pedestrian conditions, whereas the Realizable suggests a less comfortable pedestrian environment.

A flow physics study using surface shear stream-traces and Q-criterion analysis showcased the unsteady properties of each model in terms of predicting separation and reattachment along with the intensity of the flow features. We observe that the k–ϵ Standard model predicts intense and early separation off the sides leading to a larger wake region behind the reattachment point, while the Realizable was the second in terms of predicting higher intensity separation off the sides, and RNG being the weakest amongst them. On the other hand, when the flow separation from the roof is analyzed it is observed that the RNG model predicts immediate separation leading to the creation of vortical structures on the hipped roof along with a wider and larger separation region on top of the model, while the standard model predicted a delayed separation and hence a weaker region of separated airflow above the model with shifted spiral Stable Focus points down the sides of the modelthat led to the intense side separation. We find that the Realizable model predicts the side vortex to be a result of both the horseshoe vortex and the flow deflected off of it, which is not the case of the other two models as they predicted side vortex flow to be originating through the deflected flow only. Since building surface pressure distributions are correlated with the predicted aerodynamic features of the turbulence models, we recommend that future practitioners conduct parametric studies using multiple turbulence models when contrasting results with building standards. It is also recommended that future studies consider providing an explicit comparison with industrial building standards in order to proliferate the usage of CFD in combination with wind tunnel testing.Because CFD can reveal extensive aerodynamic detail, building a portfolio of these three analysis techniques may help to improve the overall reliability of computational wind engineering. Since the results presented herein are geographically and geometrically independent, they are therefore case-specific and a larger data set should be ascertained. A final limitation of the present work concerns the lack of validation between CFD results and an existing experimental data set. This is an important consideration that will be addressed in future work to enhance the validation of the CFD methodology presented.

Acknowledgments

This research did not receive any specific grant from funding agencies in the public, commercial, or non-profit sectors.

References

Abdelfatah, N., Elawady, A., Irwin, P. and Gan, A. (2022), "Experimental investigation of wind impact on low-rise elevated residences", *Eng. Struct.*, **257**(January), 114096. https://doi.org/10.1016/j.engstruct.2022.114096.

Amini, M. and Memari, A.M. (2021), "LES simulations of wind-induced pressure on the floor system underside of elevated buildings", *Wind Struct.*, **33**(5), 397-407. https://doi.org/10.12989/was.2021.33.5.397.

Blocken, B. (2014), "50 years of Computational Wind Engineering: Past, present and future", *J. Wind Eng. Ind. Aerod.*, **129**, 69-102. https://doi.org/10.1016/j.jweia.2014.03.008.

Blocken, B. (2018), *LES over RANS in Building Simulation for Outdoor and Indoor Applications: A foregone Conclusion?*, **11**(5), 821-870. https://doi.org/10.1007/s12273-018-0459-3.

British Standards Institution (2002), *BS 6399-2: Loading for Buildings — Part 2: Code of Practice for Wind Loads*, Technical Report, British Standards Institute.

British Standards Institution (2005), *BS EN 1991 1-4: Eurocode 1: Actions on Structures - Part 1-4: General Actions - Wind Actions*, Technical report, British Standards Institute.

British Standards Institution (2010), *BS NA EN 1991-1-4: UK National Annex to Eurocode 1. Actions on Structures. General Actions. Wind Actions*, Technical Report, British Standards Institute.

Crasto, G. (2007), *Numerical Simulations of the Atmospheric Boundary Layer*, Ph.D. Dissertation, University of Cagliari.

Fernando, S., Fernando, S. and Mendis, P. (2020), "Pedestrian wind comfort study using Computational Fluid Dynamic (CFD) simulation", **44**(2013), 323-339. https://doi.org/10.1007/978-981-13-9749-3_30.

Han, Y., Shen, L., Xu, G., Cai, C.S., Hu, P. and Zhang, J. (2018), "Multiscale simulation of wind field on a long-span bridge site in mountainous area", *J. Wind Eng. Ind. Aerod.*, **177**, 260-274. https://doi.org/10.1016/j.jweia.2018.04.012.

Hargreaves, D.M. and Wright, N.G. (2007), "On the use of the k-epsilon model in commercial CFD software to model the neutral atmospheric boundary layer", *J. Wind Eng. Ind. Aerod.*, **95**(5), 355-369. https://doi.org/10.1016/j.jweia.2006.08.002.

Janssen, W.D., Blocken, B. and van Hooff, T. (2013), "Pedestrian wind comfort around buildings: Comparison of wind comfort criteria based on whole-flow field data for a complex case study", *Build. Environ.*, **59**, 547-562. https://doi.org/10.1016/j.buildenv.2012.10.012.

Juretić, F. and Kozmar, H. (2013), "Computational modeling of

the neutrally stratified atmospheric boundary layer flow using the standard k-ϵ turbulence model", *J. Wind Eng. Ind. Aerod.*, **115**, 112-120. https://doi.org/10.1016/j.jweia.2013.01.011.

Krajnović, S. and Davidson, L. (2005), "Flow around a simplified car, part 2: Understanding the flow", *J. Fluids Eng.*, **127**, 919-928. https://doi.org/10.1115/1.1989372.

Liu, S., Pan, W., Zhao, X., Zhang, H., Cheng, X., Long, Z. and Chen, Q. (2018), "Influence of surrounding buildings on wind flow around a building predicted by CFD simulations", *Build. Environ.*, **140**(May), 1-10. https://doi.org/10.1016/j.buildenv.2018.05.011.

Martinuzzi, R. and Tropea, C. (1993), "The flow around surface-mounted, prismatic obstacles placed in a fully developed channel flow", *J. Fluids Eng.*, **115**, 85-92. https://doi.org/10.1115/1.2910118.

Mittal, H., Sharma, A. and Gairola, A. (2018), "A review on the study of urban wind at the pedestrian level around buildings", *J. Build. Eng.*, **18**, 154-163. https://doi.org/10.1016/j.jobe.2018.03.006.

Montazeri, H. and Blocken, B. (2013), "CFD simulation of wind-induced pressure coefficients on buildings with and without balconies: Validation and sensitivity analysis", *Build. Environ.*, **60**, 137-149. https://doi.org/10.1016/j.buildenv.2012.11.012.

Oberkampf, W.L. and Trucano, T.G. (2002), "Verification and validation in computational fluid dynamics", *Progress Aeros. Sci.*, **38**, 209-272.

Ozmen, Y., Baydar, E. and van Beeck, J.P. (2016), "Wind flow over the low-rise building models with gabled roofs havingdifferent pitch angles", *Build. Environ.*, **95**, 63-74. https://doi.org/10.1016/j.buildenv.2015.09.014.

Perén, J.I., van Hooff, T., Leite, B.C. and Blocken, B. (2015), "Impact of eaves on cross-ventilation of a generic isolated leeward sawtooth roof building: Windward eaves, leeward eaves and eaves inclination", *Build. Environ.*, **92**, 578-590. https://doi.org/10.1016/j.buildenv.2015.05.011.

Richards, P.J. and Hoxey, R.P. (1993), "Appropriate boundary conditions for computational wind engineering models using the k-epsilon turbulence model", *J. Wind Eng. Ind. Aerod.*, **46-47**(C), 145-153. https://doi.org/10.1016/0167-6105(93)90124-7.

Richards, P.J. and Norris, S.E. (2011), "Appropriate boundary conditions for computational wind engineering modelsrevisited", *J. Wind Eng. Ind. Aerod.*, **99**(4), 257-266. https://doi.org/10.1016/j.jweia.2010.12.008.

Roache, P.J. (2009), *Fundamentals of Verification and Validation*, Hermosa Publishers.

Stathopoulos, T. (2006), "Pedestrian level winds and outdoor human comfort", *J. Wind Eng. Ind. Aerod.*, **94**(11), 769-780. https://doi.org/10.1016/j.jweia.2006.06.011.

Steinbrenner, J.P. and Abelanet, J.P. (2007), "Anisotropic tetrahedral meshing based on surface deformation techniques", In "45th AIAA Aerospace Sciences Meeting and Exhibit". https://doi.org/10.2514/6.2007-554.

Stull, R.B. (1988), *An Introduction to Boundary Layer Meteorology*, Springer Science + Business Media.

Tominaga, Y., ichi Akabayashi, S., Kitahara, T. and Arinami, Y. (2015), "Air flow around isolated gable-roof buildings with different roof pitches: Wind tunnel experiments and CFD simulations", *Build. Environ.*, **84**, 204-213. https://doi.org/10.1016/j.buildenv.2014.11.012.

Tominaga, Y., Mochida, A., Murakami, S. and Sawaki, S. (2008a), "Comparison of various revised k-ϵ models and LES applied to flow around a high-rise building model with 1:1:2 shape placed within the surface boundary layer", *J. Wind Eng. Ind. Aerod.*, **96**(4), 389-411. https://doi.org/10.1016/j.jweia.2008.01.004.

Tominaga, Y., Mochida, A., Yoshie, R., Kataoka, H., Nozu, T., Yoshikawa, M. and Shirasawa, T. (2008b), "AIJ guidelines for practical applications of CFD to pedestrian wind environment around buildings", *J. Wind Eng. Ind. Aerod.*, **96**, 1749-1761. https://doi.org/10.1016/j.jweia.2008.02.058.

Tominaga, Y. and Stathopoulos, T. (2009), "Numerical simulation of dispersion around an isolated cubic building: Comparison of various types of k-ϵ models", *Atmos. Environ.*, **43**(20), 3200-3210. https://doi.org/10.1016/j.atmosenv.2009.03.038.

van Druenen, T., van Hooff, T., Montazeri, H. and Blocken, B. (2019), "CFD evaluation of building geometry modifications to reduce pedestrian-level wind speed", *Build. Environ.*, **163**(April), 106293. https://doi.org/10.1016/j.buildenv.2019.106293.

Xu, X., Yang, Q., Yoshida, A. and Tamura, Y. (2017), "Characteristics of pedestrian-level wind around super- tall buildings with various configurations", *J. Wind Eng. Ind. Aerod.*, **166**, 61-73. https://doi.org/10.1016/j.jweia.2017.03.013.

Yang, Y., Gu, M., Chen, S. and Jin, X. (2009), "New inflow boundary conditions for modelling the neutral equilibrium atmospheric boundary layer in computational wind engineering", *J. Wind Eng. Ind. Aerod.*, **97**(2), 88-95. https://doi.org/10.1016/j.jweia.2008.12.001.

Zheng, X., Montazeri, H. and Blocken, B. (2020), "CFD simulations of wind flow and mean surface pressure for buildings with balconies: Comparison of RANS and LES", *Build. Environ.*, **173**(February), 106747.

2022-06-25

A 3D CFD analysis of flow past a hipped roof with comparison to industrial building standards

Khalil, Khalid

Techno Press

Khalil K, Khan H, Chahar D, et al., (2022) A 3D CFD analysis of flow past a hipped roof with comparison to industrial building standards. Wind and Structures, Volume 34, Issue 6, June 2022, pp. 483-497

https://doi.org/10.12989/was.2022.34.6.483